Progress in Physics of Applied Materials 2 (2022) 123–131

Semnan University

Progress in Physics of Applied Materials

journal homepage: https://ppam.semnan.ac.ir/

Photocatalytic activity of the $La_{.7}Ca_{0.3}MnO_3$ nanorods

A. Arabi[1], M. Fazli[1,*], M. H. Ehsani[2,*]

[1] *Department of Chemistry, Semnan University, Semnan, 35195-363, Iran*
[2] *Department of Physics, Semnan University, Semnan, 35195-363, Iran*

ARTICLE INFO

Article history:
Received: 16 November 2022
Revised: 13 December 2022
Accepted: 17 December 2022

Keywords:
Hydrothermal
$La_{0.7}Ca_{0.3}MnO_3$
Photocatalysis
Adsorption
hybrid process
Rhodamine B

ABSTRACT

$La_{0.7}Ca_{0.3}MnO_3$ (LCMO) powder was synthesized via the hydrothermal method. Structural, morphological, and optical properties of the as-prepared sample were systematically characterized. The XRD results proved the existence of only one crystalline phase. The FESEM image indicates that the $La_{0.7}Ca_{0.3}MnO_3$ sample has a nanorod structure with an average diameter of approximately 125 nm. According to UV-Vis analysis, the band gap energy of the sample was estimated about 2.13 eV. The adsorption and photocatalytic performances of LCMO nanostructure were systematically characterized. The photoactivity efficiency for decolorizing Rhodamine B solution (10 ppm), by LCMO (0.5 g/L), with nearly 80 min illumination, was more than 90% with a reaction rate constant of 0.029 min^{-1}. Ultimately, the reusability of the photocatalyst for degrading the RhB dye was investigated using six cycles. The good reusability and stability of LCMO implies a potential application for dealing with high-concentration dyes by adsorption–photocatalytic degradation.

1. Introduction

One of the major groups of pollutants, produced as a result of industrial processes, is considered to be colored dye wastewater [1,2]. The continuous release of industrial pollutants may create severe difficulties for human activities and aquatic life [3,4]. Nowadays, modern techniques, for instance, advanced oxidation processes (AOPs), are used for solving these problems [5]. Among AOPs techniques, the use of heterogeneous photocatalysts is a cheap, easy, and efficient way to degrade organic contaminants such as dyes and pharmaceutical pollutants from industrial processes and non-toxic products, respectively [6,7] Heterogeneous Photocatalysis is a promising science in future applications which combines the topics of materials science, nanotechnology, energy research, environmental science, photonics, and chemical analysis.

Among the photocatalysts, Titanium dioxide (TiO_2) and Zinc oxide (ZnO) are the best applied materials. However, possessing a large band gap restricts their application in all irradiation spectrums. So that they only degrade organic pollutants under ultraviolet (UV) irradiation. As a result, good substitutions are essential to overcome these limitations [9,10]. Previous studies of our photocatalysis research group had been devoted to photocatalytic degradation of reactive dye and pharmaceuticals by TiO_2, and its nanocomposites exposed to UV irradiation [7-12].

In the photodegradation process, initial high adsorption of contaminates on the surface of the catalyst is essential for achieving highly efficient photodegradation [13-21]. Furthermore, high initial adsorption can enhance the photodegradation rate [22]. Higher degradation was achieved in the simultaneous adsorption/photocatalysis system (A+P) compared to the individual adsorption or photocatalysis mechanism [23]. For this reason, a combination of adsorption and photocatalysis has attracted increasing attention [24-30]. It is significant to develop materials with the double purpose of high adsorption and good photocatalytic activity. Modification of photocatalysts efficiency using catalysts or doping instead of inert adsorbents is more reasonable and practical, leading to a better result. In this regard, Calcium doped lanthanum manganite (LCMO) exhibits good adsorption ability and photocatalytic activity for some contaminant molecules thanks to their unique characteristics.

* Corresponding author
E-mail address: mfazli@semnan.ac.ir and Ehsani@semnan.ac.ir

DOI: 10.22075/ppam.2022.29008.1041

The properties of $La_{1-x}A_xMnO_3$ perovskite-type oxides are dependent on the precursor's stoichiometry, the average ionic radius of the substituted element (tolerance factor), and the amount of substitution instead of lanthanum (x content) [31].

$La_{1-x}Ca_xMnO_3$ compound is utilized in many applications such as magnetic information storage, low and high magnetic field sensors, magnetocaleric, thermoelectric, photocatalyst, and so on [32,33].

In this research, initially, we prepared the $La_{0.7}Ca_{0.3}MnO_3$ nanostructures via the ultrasonic assisted mild hydrothermal method. Then the single adsorption ability (A), photocatalytic activity (P), and integrated process based on the combination of adsorption and photocatalysis (A/P and A+P systems) of obtained powder were used for the photodegradation of Rhodamine B as a basic dye (Triphenylmethane) in darkness and under visible LED light irradiation as a light source.

In recent years, LED light sources have been used increasingly because of being cost-effective, environmentally friendly, and sustainable sources [34]. LEDs have several advantages such as low warm-up time, stability and easy handling, operation at low voltage, low power requirement, and extraordinary lifetime compared to incandescent and fluorescent lamps [35].

So far, visible LED light sources, along with photocatalysts have been successfully used for the degradation of dyes like Methylene Blue, Rhodamine B, and Congo Red in an aqueous medium [36].

To the best of our knowledge, this research is the first report on $La_{0.7}Ca_{0.3}MnO_3$ compound applied by our research group for decolorizing RhB dye via adsorption and photocatalysis under visible LED light irradiation as an individual, simultaneous and consecutive candidate.

2. Experimental

Analytical grade $KMnO_4$, $MnCl_2.4H_2O$, $La(NO_3)_3.4H_2O$, $Ca(NO_3)_2.4H_2O$, KOH, Rhodamine B (RhB), acetic acid, sodium acetate, ammonium hydroxide, and ammonium chloride were purchased from Merck company and used without any purification. Additionally, high- purity water from a Milli-Q-Water System (Millipore, Bedford, MA, USA) was utilized for the preparation of all solutions and suspensions.

The $La_{0.7}Ca_{0.3}MnO_3$ powder was synthesized via ultrasonic-assisted mild hydrothermal method using an appropriate molar concentration of metal cation based on stoichiometry ratios the same as our previous research [18]. Based on the existing relation, the contents of the molar concentration of reactants, and the initial molar ratios of initial precursors for the synthesis of $La_{0.7}Ca_{0.3}MnO_3$ were evaluated to be $0.3MnO_4^-$:$0.7Mn^{2+}$:$0.7La^{3+}$:$0.3Ca^{2+}$:606KOH:$1682H_2O$. The molar ratio of the participating manganese salts was calculated based on the valences of the reactants to obtain the desired average manganese oxidation state of 4^+ in the reactant mixture. The KOH solution was added as a mineralizer to adjust the pH of the solution to 14. The first step in the synthesis of calcium-doped manganite is adding an appropriate volume of La^{3+}, Ca^{2+}, and Mn^{2+} fresh solution, respectively, into a 200 ml glass container with a lid and then ultrasonicated for 10 minutes (in an ultrasonic bath working at 50/60 kHz of frequency (SW3, Switzerland)). After that, KOH solution was added to the obtained homogeneous solution, and finally, the MnO_4^- solution was added to the as-prepared solution. To get a homogeneous black solution, the ultimate solution was ultrasonicated for 30 minutes and then poured into a 200 ml Teflon vessel occupying 55% of its volume. Then the vessel was sealed in a stainless-steel autoclave for hydrothermal treatment. The crystallization reaction was performed at 200 ˚C under autogenous pressure for 24 h. After the autoclave was cooled down to room temperature naturally, the precipitated sample was separated, precisely washed, and neutralized by mixing in diluted acetic acid solution and a large amount of deionized water, respectively, and then dried at 120 ˚C overnight. Finally, on the basis of the thermogravimetric analysis result, the obtained powder was calcined in a muffle furnace at 850 ˚C for six hours.

The structural, spectroscopic, and optical properties of the resulting powders have been investigated by TGA, XRD, FE-SEM, FT-IR, and UV-Visible techniques. The adsorption ability and removal efficiency of the as-prepared nanostructure powders were examined on the Rhodamine B dye as a model of the pollutant from aqueous solutions. Also, the photocatalytic activity of the synthesized powder was evaluated on the aqueous solution of RhB under visible LED light irradiation at room temperature. More importantly, for the first time, the individual and simultaneous adsorption and photodegradation behaviors of RhB aqueous solution were investigated under visible light irradiation using LCMO.

Visible full spectrum LED lamps (1 W, 350 mA, Luminous intensity: 130-140 lm) were equipped with multi-chip arrays of Visible LEDs with the equivalent wavelength of 380-840 nm. Visible LEDs were purchased from (LMD-1 W White J 45 A 1, China). They were packaged in a standardized transistor with an internal heat sink for heat dissipation. Using a multi-chip array of Visible LEDs leads to higher intensities compared to conventional array configuration. A 60 mm crystallizer was used as a photoreactor placed under the visible LED lamps. The reactor was continuously mixed with a magnetic stirrer. Figure 1 shows the schematic diagram of the circuit connection of visible LED lamps. Fifteen full spectrum white LEDs were soldered to a circular-shaped programmable circuit board. An aluminum circular disk was used as a heat sink to transfer heat from visible LEDs. LEDs were powered by a homemade constant-current power supply (KORAD KA3005D, Walpole, MA, USA). The distance between the surface of the solution in the photoreactor and the LEDs was 5 cm.

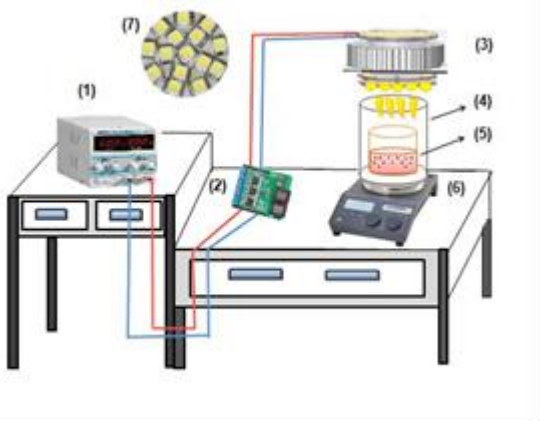

Fig. 1. Schematic of a LED photoreactor including: (1) DC power supply, (2) LED modules, (3) aluminum heat sink, (4)cylindrical mirror, (5) crystallizer, (6) magnetic stirrer and (7) LED array.

3. Structural and Spectroscopic Characterization

Thermogravimetric analysis of the dried sample and phase formation of the as-prepared sample ($La_{0.7}Ca_{0.3}MnO_3$) was characterized using an STA PT 1600, LINSEIS instrument (made in Germany). The experiments were carried out under atmospheric conditions at a heating rate of 5 °C min^{-1} up to 1000 °C. The obtained sample was calcined and then its XRD pattern was attained using a Philips PW 1710 X-ray diffractometer, with Cu Kα radiation (λ = 0.15418 nm). XRD pattern was recorded in the 2θ range of 20–80 degree at room temperature, with a 2θ step size of 0.05 degree and a time per step of 5 s. Rietveld refinement was performed with FULLPROF software for the diffraction peak patterns.

The Fourier Transform Infrared Spectroscopy (FT-IR) was recorded by an FT-IR 8400 S, Shimadzu (made in Japan and active in Semnan University) spectrophotometer in the region of 4000 – 400 cm^{-1} with a scan resolution of 2 cm^{-1} using KBr pellets. The morphology of the $La_{0.7}Ca_{0.3}MnO_3$ nanorods was examined by Mira 3-XMU Field Emission Electron Scanning Microscope (FESEM) (active in Semnan University). Optical properties, for instance, band gap of the sample, were analyzed using UV-Visible Diffuse Reflectance Spectrophotometer (PG Instruments, UK and active in Semnan University). Finally, electronic absorption spectra were recorded by a UV-16500 PC, Shimadzu (Japan) double-beam spectrophotometer.

4. Results and discussion

4.1. Structural and optical properties

The acquired TGA curve for the as-prepared specimen, from the hydrothermal process at heating rates of 5 ˚C min^{-1} from 25 to 1000 ˚C, is provided in Figure 2. The calcination temperature of the sample is calculated by the results related to the TGA analysis. The same TGA results by Daengsakul [37]. It is found that at the approximate temperature of 650°C, the perovskite oxide phase formation is being appeared and lasted at 800°C. This observation is in accordance with the XRD analyses. The same conclusion has also been reported by Wenwei [38].

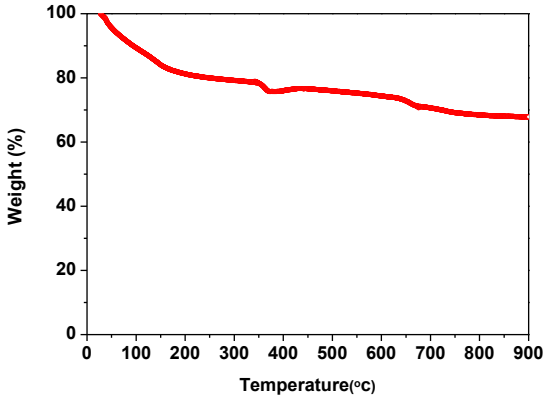

Fig. 2. TGA measurement for the hydrothermal obtained powder.

By grinding and then calcining with regard to TGA results (5 ˚C/min), the doped manganite perovskite has resulted. The related XRD pattern is found to be in the orthorhombic perovskite structure within the Pnma space group. No sign of a secondary phase was detected, exhibiting the well-crystallization of the perovskite-type structure. Using the FULLPROF software, the structural parameters of the sample were refined. The Rietveld refinement was utilized for obtaining the lattice parameters, bond length, and bond angles between Mn and O in the octahedral cage (MnO_6) by fitting the obtained XRD pattern with a crystal model based on mathematical approximation. Both the experimental and refined XRD patterns are demonstrated in Figure 3. The structural parameters and fitting factor values, which agree with the previously reported values [39], are provided in Table 1.

In Figure 4, the FT-IR spectrum of $La_{0.7}Ca_{0.3}MnO_3$ compound is depicted. There are two absorptions, and active bands around 600 and 400 cm^{-1}. The higher frequency band at 602 cm^{-1} is pertained to the stretching mode (ν_s) in the Mn–O–Mn or Mn–O bonds, which results in a variation in the internal motion of Mn–O bond length [40]. While the corresponding band of 409 cm^{-1} is related to the variations in the Mn–O–Mn bond angle. These two bands are pertained to the environment surrounding of the MnO_6 octahedral in the ABO_3 perovskite, indicating the formation of perovskite structure of the $La_{0.7}Ca_{0.3}MnO_3$, which is in agreement with the XRD results [41]. It is worth remarking that the Mn–O–Mn bond length, and the angle is found to be the result of small difference in ν_s and ν_b values, which are acquired by the structural refinement (Table 1). Furthermore, the extra peaks are related to $KBr(H_2O)_n$ and CO_2 corresponding to the wave numbers of about 1550 and 2350 cm^{-1}, respectively, existing in the ambient conditions.

By FESEM technique the morphological image of the synthesized $La_{0.7}Ca_{0.3}MnO_3$ nanorods is provided, and shown in Figure 5. The uniform distribution monodisperse nanorods with typical lengths in the range of micrometers are estimated for the sample.

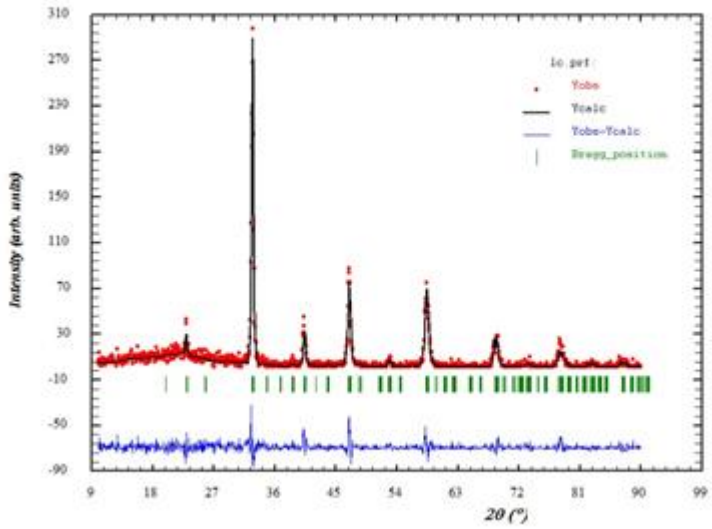

Fig. 3. Room temperature XRD pattern of the sample (red symbol) and Rietveld profile file (black line).

Table 1. Structural parameters obtained by Rietveld refinement method.

a (A °)	b (A °)	c (A °)	V (A °3)	GOF	d_{Mn-O}(A °)	θ_{Mn-O}(°)	D(nm)
5.4548	7.7552	5.4887	232.1888	1.055	1.947	169.48	23.02

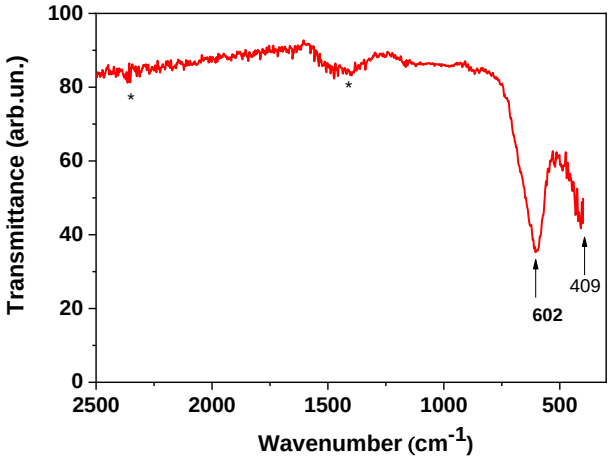

Fig. 4. FT-IR spectrum of $La_{0.7}Ca_{0.3}MnO_3$ nanorods.

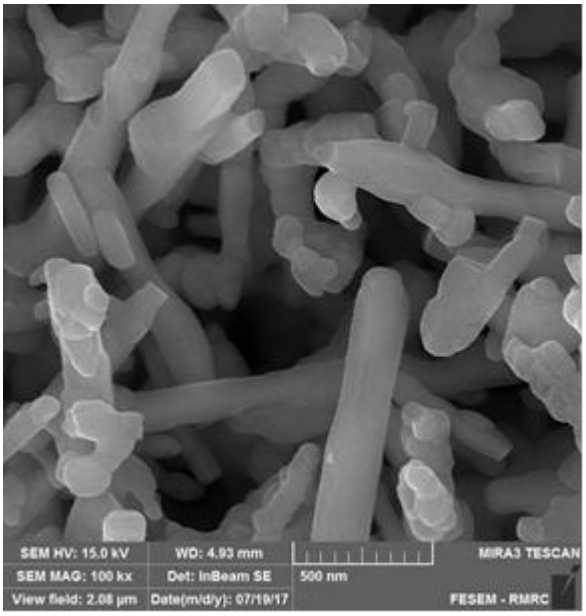

Fig. 5. Scanning electron microscopy image of the $La_{0.7}Ca_{0.3}MnO_3$ sample.

Some factors such as the manganese and metals precursors, hydrothermal conditions, concentration of mineralizer, and the mechanism of crystal growth make an impression on the morphology of the as-synthesized products [42].

Due to the significance of the photocatalytic applications of the $La_{0.7}Ca_{0.3}MnO_3$ in the photodegradation processes, its optical absorption spectrum is presented in Figure 6 Semiconductors with high band gaps, which are sensitive to the Ultraviolet spectrum, are less efficient than the ones with lower band gaps for the visible spectrum. As a result, various approaches have been investigated to reduce the band gap of UV-active semiconductors in order to overlap them with the solar spectrum.

$LaMnO_3$, as a parent compound, has an antiferromagnetic insulating ground state with four 3d electrons in a high spin configuration, i.e. $t_{2g}^3eg^1$. Mn^{4+} ions can be resulted from a La substitution with a divalent cation [43]. Therefore, the $La_{0.7}Ca_{0.3}MnO_3$ compound is interpreted to belong to the hole doped manganite perovskites. Although $LaMnO_3$ is rich in Mn^{3+}, the key role of the mixed valence of Mn^{3+} and Mn^{4+} in the $La_{0.7}Ca_{0.3}MnO_3$ ($La^{3+}_{0.7}Ca^{2+}_{0.3}Mn^{3+}_{0.7}Mn^{4+}_{0.3}O_3$) in its electronic structure cannot be ignored.

The settlement of Mn-site at the center, being surrounded by six oxygen atoms, leads to the formation of an octahedral structure, in addition to the location of La/Ca cations located at the corners, results in the formation of a cubic lattice structure. As a result of the crystal field (CF) energy, division of the low lying narrower t_{2g} triplet and high-lying broader e_g doublet sub-bands from the five Mn-3d orbitals are possible. Then because of the exchange interaction, all of the e_g sub-bands are also divided into up and down-spin bands. The two-fold degenerate e_g levels (e_{1g} and e_{2g}) are free from the Mn^{4+} ion which are occupied by an electron with a spin parallel to the core spin of the Mn^{3+} ion.

In the $La_{0.7}Ca_{0.3}MO_3$, various charge transitions, for instance, $Mn^{3+}(e_{1g}) \rightarrow Mn^{3+}(e_{2g})$, $Mn^{3+}(e_{1g}) \rightarrow Mn^{4+}(e_g)$, $O^{2-}(2p) \rightarrow Mn^{3+}(e_{2g})$, $O^{2-}(2p) \rightarrow Mn^{4+}(e_g)$ are found to be existed. Meanwhile, some physical rules including parity and spin polarity are considered to be impressive in the prohibition of the charge transfer citations in $t_{2g} \rightarrow e_g$ and $eg \rightarrow eg$. The occurrence of these transitions are assigned to the spin–orbit coupling, lattice distortions/disorder, and mixing of odd parity wave functions [44]. Three obvious peaks in Figure 6 are attributed to the optical response of the $La_{0.7}Ca_{0.3}MnO_3$ sample. The first peak is observed around 235 nm (5.2 eV), the second one is seen at 325 - 380 nm wavelength (3.8-3.3 eV), and the third one occurs around 950 nm (1.3 eV) for the sample.

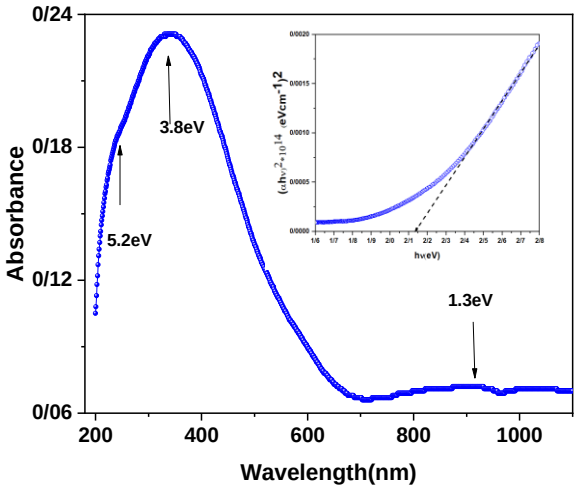

Fig.6. Room-temperature UV–vis spectra of the $La_{0.7}Ca_{0.3}MnO_3$, Inset: The plot of $(\alpha h\nu)2$ vs. photon energy ($h\upsilon$) of the $La_{0.7}Ca_{0.3}MnO_3$ nanorods.

Using Tauc's plot of $(\alpha h\nu)^2$ versus ($h\nu$) and then extrapolating the linear portion of the curve to the energy axis from the UV-Vis spectra, the band gap energy of the $La_{0.7}Ca_{0.3}MnO_3$ nanoparticles is calculated as follows [45].

$$(\alpha h\nu)^2 = A(h\nu - E_g) \quad (1)$$

where α is the absorption coefficient, E_g is the band gap energy, hυ is the photon energy, and A is a constant dependent on the effective masses of the electron, the hole, and the materials refractive index.

In the inset of Figure 6, the related Tauc plot of $La_{0.7}Ca_{0.3}MnO_3$ nanoparticles is illustrated. As observed the equivalent optical band gap of $La_{0.7}Ca_{0.3}MnO_3$ nanorods is found to be 2.13 eV.

4.2. Photocatalytic Properties of doped manganites nanorods

The photocatalytic degradation of RhB dye in aqueous solution was performed using the as-prepared LCMO sample as a photocatalyst model under low power LED visible light irradiation. The initial concentration of RhB solutions was kept constant based on similar studies conducted by researchers [46-47]. The low power LED system was kept 5 cm above and around the RhB solution surface. The first step for photocatalytic treatment of water is to define the characteristics of the contaminated water to be treated in water composition and pH [48]. The effect of pH on the degradation of the RhB has been studied and the highest efficiency of process was obtained at pH=4.5. The photodegradation of RhB solutions (10 ppm) was performed using LCMO sample (0.50 g / L) exposed to the visible LED light at different time intervals (0 – 84 min). The UV-Vis spectra of dyes in aqueous solutions after exposure to photocatalyst showed fast degradation of dyes molecules with the elapse of time. The maximum absorptions peak of RhB at 554 nm continuously decays with the illumination time, along with a change of the color of solutions from red color to colorless.

The degradation percent of the contaminated constituents [49] has been evaluated by the following equation:

$$D(\%) = \frac{A_0 - A}{A_0} \times 100 \quad (2)$$

where A_0 is the initial absorbance of the contaminated constituent in solution and A is the absorbance after photodegradation process. To simplify, the two reaction systems, including (1) equilibrium adsorption followed by photodegradation, and (2) simultaneous adsorption accomplished with photodegradation, were denoted as A/P and A+P, respectively (Fig. 7 and Fig. 8).

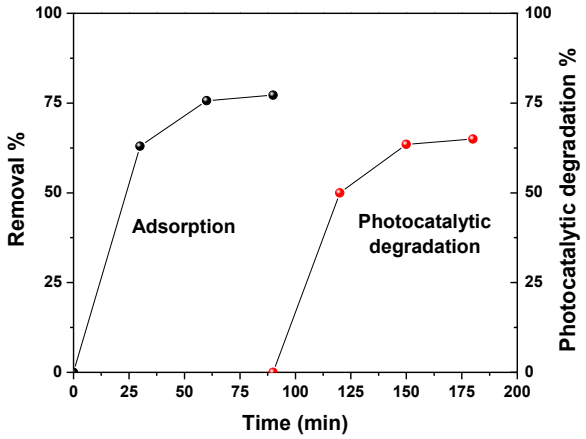

Fig. 7. Variation of RhB concentration as a function of time in A/P system over LCMO. (experimental conditions: initial RhB concentration = 10 mg/L, LCMO = 0.5 g/L, pH=4.5, T = 25 °C)

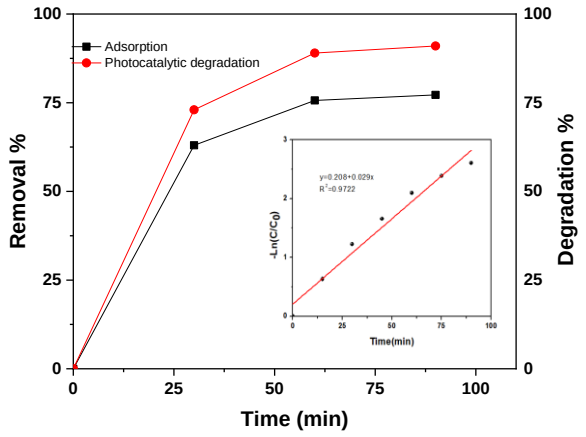

Fig. 8. Variation of RhB concentration as a function of time in the individual A and A + P systems over LCMO (Experimental conditions: initial RhB concentration = 10 mg/L, LCMO = 0.5 g/L, pH=4.5, T = 25 °C). Inst: Pseudo first order kinetics plot of RhB degradation onto the LCMO nanophotocatalyst.

Fig. 8 shows that 0.50 g / L of photocatalyst decolorizes RhB solution (10 ppm) up to 80% in 80 minutes.

In this study, the photocatalytic degradation results of RhB over LCMO are consistent with the Langmuir–Hinshelwood model [50]. Plotting – ln (C / Co) versus time represents a straight line, in which its slope upon linear regression equals to the apparent first-order rate constant, K_{app}. Inset of Figure 8 shows that the degradation of RhB follows the pseudo first-order kinetics expressed as Eq. (37):

$$r = -\frac{dC}{dt} = K_{app}C \quad (3)$$

Where K_{app} is the apparent first-order reaction rate constant and t is the reaction time. The K_{app} values give the degradation rate of RhB molecules via heterogeneous

photocatalytic reaction under LED visible light irradiation. During the photocatalytic process, the RhB molecules are adsorbed on the LCMO surface and an equilibrium time of adsorption – desorption is reached nearly 30 min. Thus, an equilibrium concentration of the RhB solution was used as the initial dye concentration for the kinetic analysis (C_0). Integrating equation (3) (with the restriction of $C = C_0$ at $t = 0$, in which C_0 is the initial concentration in the bulk solution during the dark adsorption) leads to Eq. (4):

$$-\ln\left(\frac{C_t}{C_0}\right) = K_{app}t \qquad (4)$$

……Where C_t and C_0 represent the concentration of RhB at zero time and after a reaction time t, respectively. Plotting $-\ln(C / C_0)$ versus time represents a straight line, in which its slope upon linear regression equals to apparent first-order rate constant, K_{app}. According to Eq. (4), the plot of $-\ln(C / C_0)$ versus t for all concentrations is linear. Thus, the value of K_{app} can be obtained directly via its slope. It is clear that the initial concentration of RhB has a significant effect on the degradation rates. In the lower initial concentrations, the rate constant of degradation is found to be higher. This can be justified by the finite amount of active centers on the photocatalyst as well as the excessive RhB molecules in the medium, leading to the reduction in the light adsorption capability of the catalyst. Thus, the photocatalytic process is influenced by the initial concentration of RhB.

The slope of the linear plot in the inset of Figure 8 is equal to the apparent first order reaction rate constant (K_{app}). So, this value was found to be 0.029 min^{-1} in the presence of the LCMO nanorods.

4.3. Reusability of the LCMO

The stability performance and reusability of photocatalysts and adsorbent are very impressive in economical and practical applications [51]. In the present study, the reusability of the applied LCMO powder was performed using six cycles. At the end of each process, the LCMO powders were collected and washed with 0.01 M H_2SO_4 solution followed by a sufficient amount of deionized water, respectively. The reason for choosing the above-mentioned desorption solution was to avoid possible damage of the adsorbent and/or physical changes of the structure. In each run, the reusability of the solid sample was performed on the same condition as mentioned before. As shown in Figure 9, the reusability of the applied LCMO did not significantly change during the six adsorption–desorption cycles. The obtained results show that the hydrothermally synthesized LCMO powder can retain its removal and decomposition activity for at least six cycles. The high desorption percentage may be due to the protonation of surface adsorbent with an acidic agent [52]. Therefore, LCMO can be introduced as an economical and effective adsorbent in the photocatalyst process for RhB removal from aqueous solutions in industrial applications.

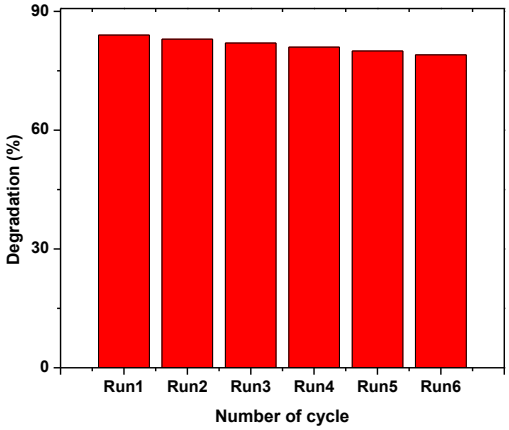

Fig. 9. Reusability of the prepared LCMO for the adsorption-photocatalytic degradation of RhB.

5. Conclusion

In this study, $La_{0.7}Ca_{0.3}MnO_3$ nanorods were synthesized by a simple ultrasonic assisted hydrothermal method followed by a heat treatment at 850 °C. XRD results showed that the obtained sample had crystalized in the perovskite structure. FESEM images showed micrometer-sized (0.05–0.22 μm) randomly distributed crystal nanorods. Using Tauc's equation, the as- prepared specimen was found to have the equivalent band gap of 2.13 eV photocatalytic activity exposed to the visible light irradiation.

It is found that the LCMO can apply as a new adsorbent. The Lagergren's pseudo-first order model exhibited the best fit for the kinetic studies, which indicates that the adsorption of RhB is limited by physisorption process. The prepared LCMO possesses a maximum adsorption capacity of 210 mg/g determined from the Langmuir isotherm. Also, LCMO shows good photocatalytic activity. The photocatalytic activity of the sample was investigated by degradation of RhB in an aqueous solution under visible LED irradiation. The photodegradation efficiency for decolorizing Rhodamine B solution (10 ppm), by LCMO (0.5 g/L), nearly 80 min illumination, was more than 90% with a reaction rate constant of 0.029 min^{-1}. The good reusability of LCMO in the cyclic removal experiments indicates that the simultaneous adsorption and photocatalytic property of LCMO is stable and practically important.

Acknowledgement

This research was partially supported by Semnan University Science and Technology Park.

References

[1] H. Jie, M. Jie, M. Jiahua, H. Huang, "Preparation of $LaMnO_3$/graphene thin films and their photocatalytic activity." Journal of Rare Earths 32 (2014) 1126-1134.

[2] N. Soltani, E. Saion, M.Z. Hussein, M. Erfani, A. Abedini, G. Bahmanrokh, M. Navasery, P.Vaziri, "Visible light-induced degradation of methylene blue in the presence of photocatalytic ZnS and CdS nanoparticles." International journal of molecular sciences 13 (2012) 12242-12258.

[3] S.A.B. Asif, S.B. Khan, A.M. Asiri, "Efficient solar photocatalyst based on cobalt oxide/iron oxide composite nanofibers for the detoxification of organic pollutants." Nanoscale research letters 9 (2014) 1-9.

[4] M. Humayun, N. Sun, F. Raziq, X. Zhang, R. Yan, Z. Li, Y. Qu, L. Jing, "Synthesis of ZnO/Bi-doped porous $LaFeO_3$ nanocomposites as highly efficient nano-photocatalysts dependent on the enhanced utilization of visible-light-excited electrons." Applied Catalysis B: Environmental 231 (2018) 23-33.

[5] S. Zou, Z. Fu, C. Xiang, W. Wu, S. Tang, Y. Liu, D. Yin, "Mild, one-step hydrothermal synthesis of carbon-coated CdS nanoparticles with improved photocatalytic activity and stability." Chinese Journal of Catalysis 36 (2015) 1077-1085.

[6] D. Rajamanickam, M. Shanthi, "Photocatalytic degradation of an azo dye Sunset Yellow under UV-A light using TiO_2/CAC composite catalysts." Spectrochimica Acta Part A: Molecular and Biomolecular Spectroscopy 128 (2014) 100-108.

[7] R.J. Tayade, T.S. Natarajan, H.C. Bajaj, "Photocatalytic degradation of methylene blue dye using ultraviolet light emitting diodes." Industrial & Engineering Chemistry Research 48 (2009) 10262-10267.

[8] W.K. Jo, "Photocatalytic oxidation of low-level airborne 2-propanol and trichloroethylene over titania irradiated with bulb-type light-emitting diodes." Materials 6 (2013) 265-278.

[9] I.K. Konstantinou, T.A. Albanis, "TiO_2-assisted photocatalytic degradation of azo dyes in aqueous solution: kinetic and mechanistic investigations: a review." Applied Catalysis B: Environmental 49 (2004) 1-14.

[10] Q.I. Rahman, M. Ahmad, S.K. Misra, M. Lohani, "Effective photocatalytic degradation of rhodamine B dye by ZnO nanoparticles." Materials Letters 91 (2013) 170-174.

[11] M. Wei, J. Wan, Z. Hu, Z. Peng, B. Wang, H. Wang, "Preparation, characterization and visible-light-driven photocatalytic activity of a novel Fe (III) porphyrin-sensitized TiO_2 nanotube photocatalyst." Applied Surface Science 391 (2017) 267-274.

[12] M.R. Eskandarian, M. Fazli, N.M. Rasoulifard, H. Choi, "Decomposition of organic chemicals by zeolite-TiO_2 nanocomposite supported onto low density polyethylene film under UV-LED powered by solar radiation." Applied Catalysis B: Environmental 183 (2016) 407-416.

[13] M.R. Eskandarian, H. Choi, M. Fazli, "Rasoulifard, M.H. "Effect of UV-LED wavelengths on direct photolytic and TiO_2 photocatalytic degradation of emerging contaminants in water." Chemical Engineering Journal 300 (2016) 414-422.

[14] M. Shaterian, M. Enhessari, D. Rabbani, M. Asghari, M. Salavati-Niasari, "Synthesis, characterization and photocatalytic activity of $LaMnO_3$ nanoparticles." Applied surface science 318 (2014) 213-217.

[15] M. Maleki, M. Haghighi, "Sono-dispersion of CuS-CdS over TiO_2 in one-pot hydrothermal reactor as visible-light-driven nanostructured photocatalyst." Journal of Molecular Catalysis 424 (2016) 283-296.

[16] G.R. Andrade, C.C. Nascimento, E.C. Neves, C.D.A.E. Santo Barbosa, L.P. Costa, L.S. Barreto, I.F. Gimenez, "One-step preparation of CdS nanocrystals supported on thiolated silica-gel matrix and evaluation of photocatalytic performance." Journal of hazardous materials 203 (2012) 151-157.

[17] D. Das, N. Biswal, S. Martha, K. Parida, "Solar-light induced photodegradation of organic pollutants over CdS-pillared zirconium–titanium phosphate (ZTP)." Journal of Molecular Catalysis A: Chemical 349 (2011) 36-41.

[18] A. Arabi, M. Fazli, M. Ehsani, "Tuning the morphology and photocatalytic activity of $La_{0.7}Ca_{0.3}MnO_3$ nanorods via different mineralizer-assisted hydrothermal syntheses." Materials Research Bulletin 90 (2017) 205-211.

[19] Y. Li, X. He, M. Cao, "Micro-emulsion-assisted synthesis of ZnS nanospheres and their photocatalytic activity." Materials Research Bulletin 43 (2008) 3100-3110.

[20] S. Fu, H. Niu, Z. Tao, J. Song, C. Mao, S. Zhang, C. Chen, D. Wang, "Low temperature synthesis and photocatalytic property of perovskite-type $LaCoO_3$ hollow spheres." Journal of Alloys and Compounds 576 (2013) 5-12.

[21] H. Yang, J. Zhang, G. Lin, T. Xian, J. Jiang, "Preparation, characterization and photocatalytic properties of terbium orthoferrite nanopowder." Advanced Powder Technology 24 (2013) 242-245.

[22] L. Xiong, W. Sun, Y. Yang, C. Chen, J. Ni, "Heterogeneous photocatalysis of methylene blue over titanate nanotubes: Effect of adsorption." Journal of colloid and interface science 356 (2011) 211-216.

[23] D. Dinda, A. Gupta, S.K. Saha, "Removal of toxic Cr (VI) by UV-active functionalized graphene oxide for water purification." Journal of Materials Chemistry A 1 (2013) 11221-11228.

[24] K. Kusakabe, M. Ezaki, A. Sakoguchi, K. Oda, N. Ikeda, "Photocatalytic behaviors of silica-loaded mesoporous titania." Chemical Engineering Journal 180 (2012) 245-249.

[25] F. Chen, Z. Liu, Y. Liu, P. Fang, Y. Dai, "Enhanced adsorption and photocatalytic degradation of high-concentration methylene blue on Ag_2O-modified TiO_2-based nanosheet." Chemical engineering journal 221 (2013) 283-291.

[26] S. Xu, J. Ng, X. Zhang, H. Bai, D.D. Sun, "Adsorption and photocatalytic degradation of Acid Orange 7 over hydrothermally synthesized mesoporous TiO_2 nanotube." Colloids and surfaces A: physicochemical and engineering aspects 379 (2011) 169-175.

[27] H.A. Le, S. Chin, J. Jurng, "Photocatalytic degradation of methylene blue by a combination of TiO_2-anatase and coconut shell activated carbon." Powder Technology 225 (2012) 167-175.

[28] D. Xu, Z.H. Huang, F. Kang, M. Inagaki, T.H. Ko, "Effect of heat treatment on adsorption performance and photocatalytic activity of TiO_2-mounted activated carbon cloths." Catalysis Today 139(2008) 64-68.

[29] M. Su, C. He, L. Zhu, Z. Sun, C. Shan, Q. Zhang, D. Shu, R. Qiu, Y. Xiong, "Enhanced adsorption and photocatalytic activity of BiOI–MWCNT composites towards organic pollutants in aqueous solution." Journal of hazardous materials 229 (2012)72-82.

[30] M. Bradha, T. Vijayaraghavan, S. Suriyaraj, R. Selvakumar, A.M. Ashok, "Synthesis of photocatalytic $La_{(1-x)}A_xTiO_{3.5-\delta}$ (A= Ba, Sr, Ca) nano perovskites and their application for photocatalytic oxidation of congo red dye in aqueous solution." Journal of Rare Earths 33 (2015) 160-167.

[31] C. Zener, "Interaction between the d-shells in the transition metals. II. Ferromagnetic compounds of manganese with perovskite structure." Physical Review 82 (1951) 403.

[32] A. Millis, B.I. Shraiman, R. Mueller, "Dynamic Jahn-Teller effect and colossal magnetoresistance in $La_{1-x}Sr_xMnO_3$." Physical review letters 77 (1996) 175.

[33] M. Culebras, R. Torán, C.M. Gómez, A. Cantarero, "$La_{1-x}Ca_xMnO_3$ semiconducting nanostructures: morphology and thermoelectric properties." Nanoscale Research Letters 9 (2014)1-5.

[34] P. Phong, D. Manh, L. Hoan, T. Ngai, N. Phuc, I.J. Lee, "Particle size effects on $La_{0.7}Ca_{0.3}MnO_3$: Griffiths phase-like behavior and magnetocaloric study." Journal of Alloys and Compounds 662 (2016) 557-565.

[35] T.M. Tank, A. Bodhaye, Y.M. Mukovskii, S.P. Sanyal, "Crystallographic direction dependence of electrical-transport, magneto-transport, magnetic and thermal properties of $La_{0.7}Ca_{0.3}MnO_3$ single crystal." Materials Research Bulletin 83 (2016) 250-258.

[36] E. Korovin, D. Selishchev, A. Besov, D. Kozlov, "UV-LED TiO_2 photocatalytic oxidation of acetone vapor: Effect of high frequency controlled periodic illumination." Applied Catalysis B: Environmental 163 (2015) 143-149.

[37] S. Daengsakul, C. Thomas, C. Mongkolkachit, S. Maensiri, "Synthesis and Structural Characterization of the $La_{0.7}A_{0.3}MnO_3$ (A= Sr, Ca, Ba and Na) Nanocrystalline Powders Prepared by a Simple Thermal Decomposition Route." Journal of superconductivity and novel magnetism 25 (2012), 2507-2518.

[38] W. Wenwei, C. Jinchao, W. Xuehang, L. Sen, W. Kaituo, T. Lin, "Nanocrystalline $LaMnO_3$ preparation and kinetics of crystallization process." Advanced Powder Technology 24 (2013) 154-159.

[39] R. Chihoub, A. Amira, N. Mahamdioua, S. Altintas, A. Varilci, C. Terzioglu, "Magnetoresistive properties of cerium doped $La_{0.7}Ca_{0.3}MnO_3$ manganites." Physica B: Condensed Matter 492 (2016) 11-15.

[40] B. Nagabhushana, R.S. Chakradhar, K. Ramesh, C. Shivakumara, G. Chandrappa, "Combustion synthesis, characterization and metal–insulator transition studies of nanocrystalline $La_{1-x}Ca_xMnO_3$ ($0.0 \leq x \leq 0.5$)." Materials chemistry and physics 102 (2007) 47-52.

[41] G.C. Lavorato, E. Lima Jr, D. Tobia, D. Fiorani, H.E. Troiani, R.D. Zysler, E.L. Winkler, "Size effects in bimagnetic $CoO/CoFe_2O_4$ core/shell nanoparticles." Nanotechnology 25 (2014) 355704.

[42] M. Anwar, F. Ahmed, B.H. Koo, "Influence of Ce addition on the structural, magnetic, and magnetocaloric properties in $La_{0.7-x}Ce_xSr_{0.3}MnO_3$ ($0 \leq x \leq 0.3$) ceramic compound." Ceramics International 41 (2015) 5821-5829.

[43] S.G. Choi, H.S. Lee, H. Choi, S.W. Chung, H.H. Park, "The effect of Sr concentration on resistive switching properties of $La_{1-x}Sr_xMnO_3$ films." Thin Solid Films 529 (2013) 352-355.

[44] M. Cesaria, A. Caricato, G. Leggieri, M. Martino, G. Maruccio, "Optical response of oxygen deficient La0. 7Sr0. 3MnO3 thin films deposited by pulsed laser deposition." Thin Solid Films 545 (2013) 592-600.

[45] S.Pazouki, N.Memarian, "Effects of Hydrothermal temperature on the physical properties and anomalous band gap behavior of ultrafine SnO_2 nanoparticles." Optik 246 (2021) 167843.

[46] X. Lin, F. Huang, W. Wang, Z. Shan, J. Shi, "Methyl orange degradation over a novel Bi-based photocatalyst Bi_3SbO_7: Correlation of crystal structure to photocatalytic activity." Dyes and Pigments 78 (2008) 39-47.

[47] H. He, J. Huang, L. Cao, J. Wu, "Photodegradation of methyl orange aqueous on $MnWO_4$ powder under different light resources and initial pH." Desalination 252 (2010) 66-70.

[48] R. Dariani, A. Esmaeili, A. Mortezaali, S. Dehghanpour, "Photocatalytic reaction and degradation of methylene blue on TiO_2 nano-sized particles." Optik 127 (2016) 7143-7154.

[49] M. Rashad, A. Ibrahim, D.Rayan, M.Sanad, I. Helmy, "Photo-Fenton-like degradation of Rhodamine B dye from waste water using iron molybdate catalyst under visible light irradiation." Environmental nanotechnology, monitoring & management 8 (2017) 175-186.

[50] M. Ghiasi, A. Malekzadeh, "Solar photocatalytic degradation of methyl orange over $La_{0.7}Sr_{0.3}MnO_3$ nano-perovskite." Separation and Purification Technology 134 (2014) 12-19.

[51] B.C. Ma, S. Ghasimi, K. Landfester, F. Vilela, Zhang, K.A. "Conjugated microporous polymer nanoparticles with enhanced dispersibility and water compatibility for photocatalytic applications." Journal of Materials Chemistry A 3 (2015) 16064-16071.

[52] S. Wang, B. Yang, Y. Liu, "Synthesis of a hierarchical SnS2 nanostructure for efficient adsorption of Rhodamine B dye." Journal of colloid and interface science 507 (2017) 225-233.